Supporting Information

Defect engineering and self-reconstruction directed stabilization of steady-state NiOOH on NiO_x for durable oxygen evolution

Chunsheng Wu [a, b], Huan Zhu [b], Hui Wang [*b], Xinran Li [*a, b] and Huan Pang [*a]

[a] School of Chemistry and Chemical Engineering, Yangzhou University, Yangzhou, 225009, China.

[b] MOE Key Laboratory of Thermo-Fluid Science and Engineering, School of Energy and Power Engineering, Xi'an Jiaotong University, Xi'an, 710049, China

E-mail: huanpangchem@hotmail.com; panghuan@yzu.edu.cn

1. Experimental section

1.1 Chemicals

Ferric (III) nitrate nonahydrate ($Fe(NO_3)_3·9H_2O$), cobalt(II) nitrate hexahydrate ($Co(NO_3)_2·6H_2O$), and DL α-alanine [$C_3H_7NO_2$] were purchased from Aladdin. Nickel acetate tetrahydrate [$Ni(CH_3COO)_2·4H_2O$] were purchased from Macklin. Absolute ethyl alcohol was purchased from Shanghai Yonghua. All aqueous solutions were freshly prepared with deionized water (18.2 MΩ cm).

1.2 Materials synthesis

Synthesis of NiO_x. A mixture of 0.622 g $Ni(CH_3COO)_2·4H_2O$ and 1.0 g DL-alanine was dissolved in 10 mL deionized water under continuous stirring at room temperature for 10 minutes until complete dissolution. Subsequently, 140 mL of anhydrous ethanol was added to the solution, and stirring was continued for an additional 5 minutes to form a blue suspension. The precipitate was isolated via centrifugation, air-dried to obtain the nickel-alanine complex, and then subjected to calcination in an air atmosphere. The calcination process involved heating the complex to 600 °C at a ramp rate of 1 °C / min, maintaining this temperature for 2 hours, and allowing the sample to cool naturally to room temperature, yielding the final powdered product.

Preparation of $pNiO_x$, $oNiO_x$, and $rNiO_x$. A homogeneous mixture containing 1 mg NiO_x powder, 200 μL anhydrous ethanol, and 10 μL Nafion was drop-cast onto a carbon paper substrate (1 × 1 cm^2) and dried to achieve a NiO_x loading of 1 mg cm^{-2}. The electrochemical reconstruction of NiO_x was conducted in a three-electrode system immersed in 1 M KOH electrolyte, with a carbon rod serving as the counter electrode, a Hg/HgO electrode as the reference electrode, and NiO_x-loaded carbon paper (1 mg cm^{-2}) as the working electrode. Three distinct electrochemical protocols were employed: (1) Pulsed potential reconstruction ($pNiO_x$): Cyclic potential pulses

alternating between a cathodic potential (Ec = -2 V vs. Hg/HgO, 1 s) and an anodic potential (Ea = 2 V vs. Hg/HgO, 1 s) were applied for 50 cycles. (2) Oxidative potential reconstruction ($oNiO_x$): A constant anodic potential of 2 V vs. Hg/HgO was maintained for 100 s. (3) Reductive potential reconstruction ($rNiO_x$): A constant cathodic potential of -2 V vs. Hg/HgO was maintained for 100 s.

Preparation of $pNiO_x$-H_2SO_4, $pNiO_x$-H_2O, and $pNiO_x$-KOH. A homogeneous mixture containing 1 mg NiO_x powder, 200 μL anhydrous ethanol, and 10 μL Nafion was drop-cast onto a carbon paper substrate (1 × 1 cm^2) and dried to achieve a NiO_x loading of 1 mg cm^{-2}. The electrochemical reconstruction of NiO_x was conducted in a three-electrode system, with a carbon rod serving as the counter electrode, and NiO_x-loaded carbon paper (1 mg cm^{-2}) as the working electrode. Three distinct $pNiO_x$ electrodes were synthesized by modulating the electrolyte composition: (1) $pNiO_x$-H_2SO_4: Cyclic potential pulses alternating between a cathodic potential (E_c = -2 V vs. Hg/Hg_2SO_4, 1 s) and an anodic potential (E_a = 2 V vs. Hg/Hg_2SO_4, 1 s) were applied for 50 cycles. (2) $pNiO_x$-H_2O: Cyclic potential pulses alternating between a cathodic potential (E_c = -2 V vs. SCE, 1 s) and an anodic potential (E_a = 2 V vs. SCE, 1 s) were applied for 50 cycles. (3) $pNiO_x$-KOH: $pNiO_x$-H_2O: Cyclic potential pulses alternating between a cathodic potential (E_c = -2 V vs. Hg/HgO, 1 s) and an anodic potential (E_a = 2 V vs. Hg/HgO, 1 s) were applied for 50 cycles.

Preparation of Fe/Co-doped $pNiO_x$. The Fe/Co-doped $pNiO_x$ electrodes were fabricated via an electrodeposition method. First, $Fe(NO_3)_3 \cdot 9H_2O$ and $Co(NO_3)_2 \cdot 6H_2O$ were dissolved in deionized water under magnetic stirring until a homogeneous solution was achieved, with a total metal ion concentration of 0.15 M (individual ion concentrations are provided in Table S1). Electrodeposition was performed in a three-electrode system using the pre-reconstructed $pNiO_x$ electrode as the working electrode, a carbon rod as the counter electrode, and a saturated calomel electrode (SCE) as the reference electrode. A constant potential of -1 V vs. SCE was applied for 20 minutes to drive the deposition process. The resulting electrodes were

sequentially rinsed with deionized water and ethanol to remove residual impurities, followed by drying in an oven at 60°C for 12 hours to obtain the final Fe/Co-doped $pNiO_x$ electrodes.

Table S1 Metal ion concentrations in deposition solutions for respective Fe/Co-doped $pNiO_x$ catalysts.

	Co / mol L^{-1}	Fe / mol L^{-1}
Co-$pNiO_x$	0.15	/
Fe-$pNiO_x$	/	0.15
Co_2Fe_1-$pNiO_x$	0.1	0.05
Co_1Fe_2-$pNiO_x$	0.05	0.1

1.3 Characterization

The morphological features were characterized by field emission scanning electron microscopy (FESEM, Zeiss-Supra55) and transmission electron microscope (TEM, Hitachi HT7800). Inductively coupled plasma-Mass Spectrometry (ICP-MS, Agilent 7700X, USA) analyses are used to determine the mass loading of metal species. High-angle annular dark-field scanning transmission electron microscopy (HAADF-STEM) images, energy-dispersive X-ray (EDX) elemental mapping were carried out on a double Cs-corrected FEI Themis G2 thermal-field emission microscope with a probe Cs-corrector working at 300 kV. A convergence angle of 25 mrad and a collection angle range of 38 to 200 mrad were used for imaging. X-ray diffraction (XRD) patterns were obtained using a Rigaku SmartLab 9KW with Cu-Kα radiation. XPS measurements were performed on a PHI 5000 VersaProbe III X-ray photoelectron spectrometer with Al Kα as the exciting source. Raman spectrum was conducted on LabRAM HR Evolution.

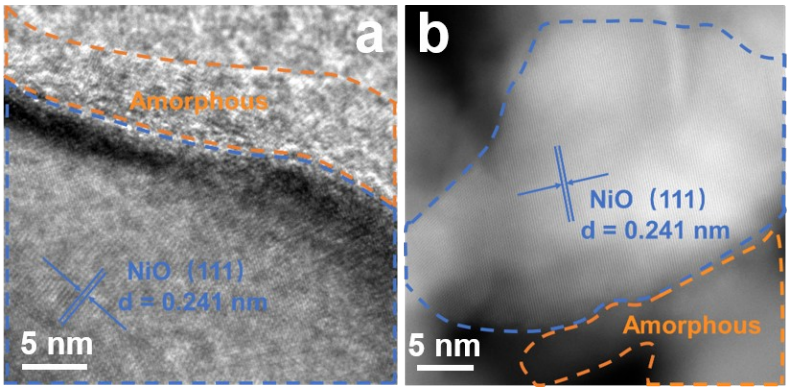

Fig. S1 (a) High-resolution TEM image of NiO_x. (b) HAADF-STEM images of $pNiO_x$.

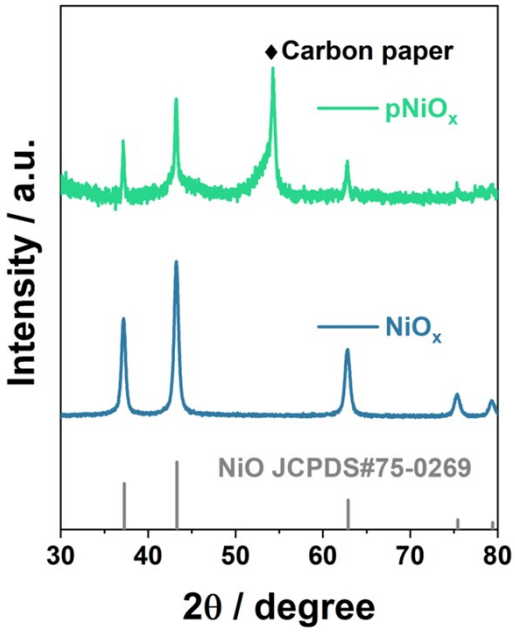

Fig. S2 XRD patterns of the as-synthesized NiO_x and $pNiO_x$.

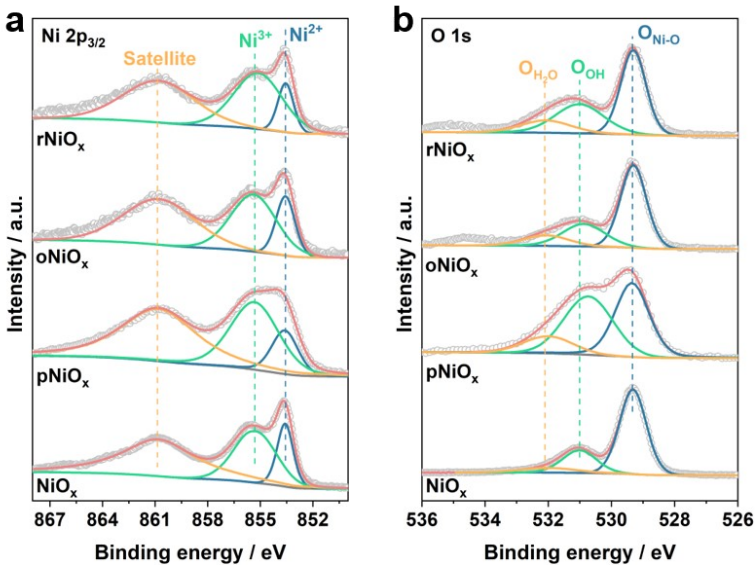

Fig. S3 (a) Ni 2p high-resolution XPS spectra and (b) O 1s high-resolution XPS spectra of NiO_x, $pNiO_x$, $oNiO_x$, and $rNiO_x$.

Table S2 Surface atomic ratios of nickel species (Ni^{3+} and Ni^{2+}) derived from Ni $2p_{3/2}$ XPS fitting of fig. 3a, and surface oxygen species (O_{Ni-O} and O_{OH}) derived from O 1s XPS fitting of fig. 3b.

	Ni^{3+} %	Ni^{2+} %	O_{Ni-O} %	O_{OH} %
NiO_x	67.96	32.04	74.65	25.35
$pNiO_x$	74.12	25.88	54.26	45.74
$oNiO_x$	69.94	30.06	69.14	30.86
$rNiO_x$	75.13	24.87	60.11	39.89

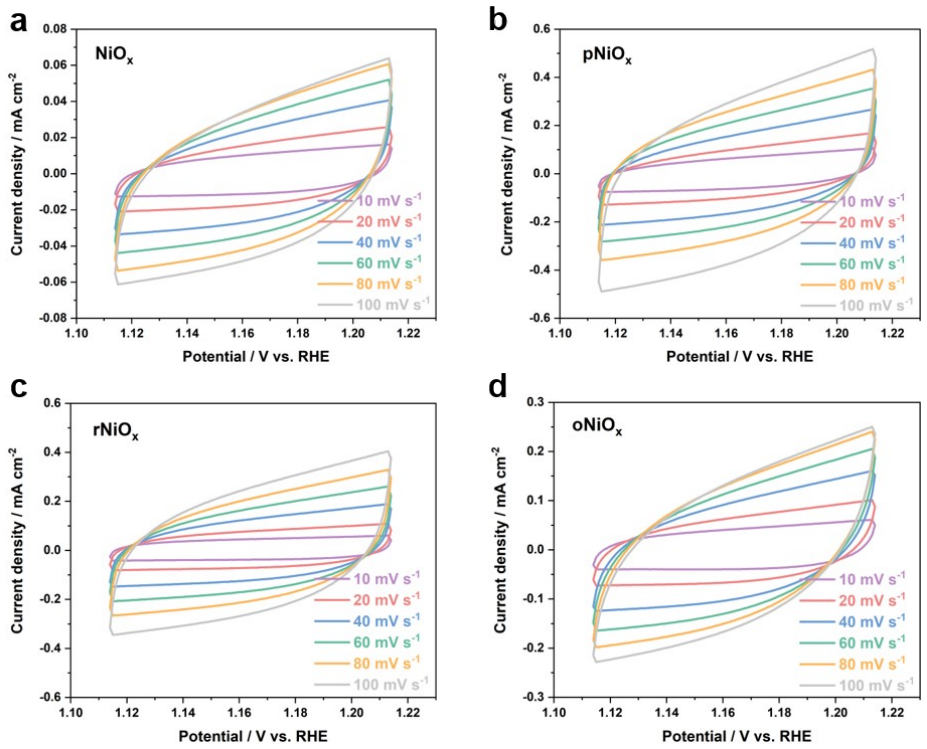

Fig. S4 CV curves of (a) NiO_x, (b) $pNiO_x$, (c) $rNiO_x$, and (d) $oNiO_x$.

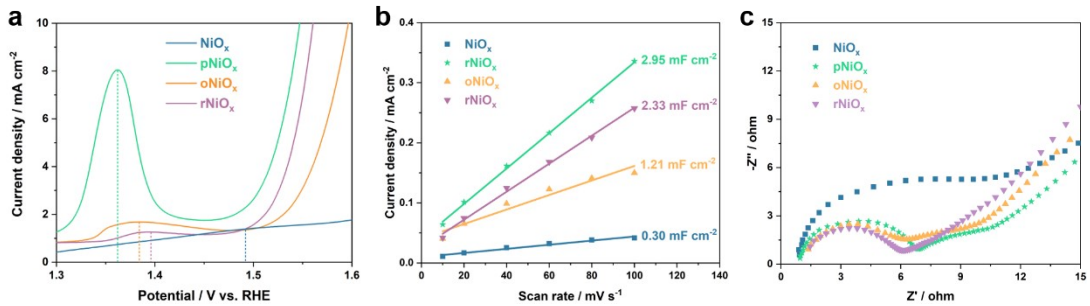

Fig. S5 (a) LSV curves, (b) C_{dl} obtained by fitting Figure S4, and (c) EIS of NiO_x, $pNiO_x$, $oNiO_x$, and $rNiO_x$.

$pNiO_x$ exhibits an oxidation peak near 1.35 V (Fig. S5a), which is attributed to the deprotonation of hydroxyl groups bonded to Ni sites, involving the oxidation of Ni^{2+} to Ni^{3+} species ($Ni(OH)_2 + OH^- \rightarrow NiOOH + H_2O + e^-$).[1] Compared to NiO_x, the oxidation peaks of all three reconstructed NiO_x samples shift negatively, indicating a reduced oxidation potential for $Ni(OH)_2$. $pNiO_x$ demonstrates the lowest oxidation potential and the largest oxidation peak area, suggesting that the conversion of $Ni(OH)_2$ to NiOOH requires minimal potential and that more $Ni(OH)_2$ is oxidized to NiOOH. These results align with the XPS analysis (Fig. S3), confirming that pulsed potentials effectively enhance the reconstruction of NiO_x into $Ni(OH)_2$/NiOOH.

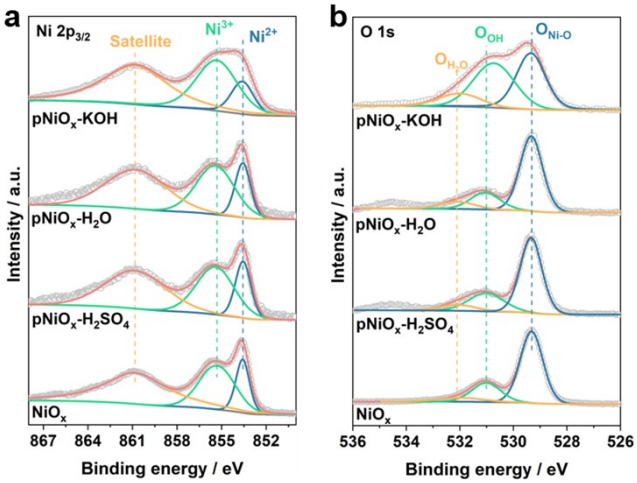

Fig. S6 (a) Ni 2p high-resolution XPS spectra and (b) O 1s high-resolution XPS spectra of NiO_x, $pNiO_x$-H_2SO_4, $pNiO_x$-H_2O, and $pNiO_x$-KOH.

To investigate the effect of electrolyte environments on the reconstruction of NiO_x under pulsed potentials, reconstructions were performed in deionized water ($pNiO_x$-H_2O), 0.5 M H_2SO_4 ($pNiO_x$-H_2SO_4), and 1 M KOH ($pNiO_x$-KOH), respectively, with their Ni 2p (Fig. S6a) and O 1s (Fig. S6b) high-resolution XPS spectra being comparatively analyzed. $pNiO_x$-KOH exhibits the largest Ni^{3+} and O_{OH} peak areas (Table S3), whereas $pNiO_x$-H_2SO_4 and $pNiO_x$-H_2O show negligible changes. These results demonstrate that OH^- promotes NiO_x reconstruction, likely forming $Ni(OH)_2$ or NiOOH.

Table S3 Surface atomic ratios of nickel species (Ni^{3+} and Ni^{2+}) derived from Ni $2p_{3/2}$ XPS fitting of fig. 2c, and surface oxygen species (O_{Ni-O} and O_{OH}) derived from O 1s XPS fitting of fig. 2d.

	Ni^{3+} %	Ni^{2+} %	O_{Ni-O} %	O_{OH} %
NiO_x	67.96	32.04	74.65	25.35
$pNiO_x$-H_2SO_4	67.35	32.65	72.01	27.99
$pNiO_x$-H_2O	68.90	31.10	77.12	22.88
$pNiO_x$-KOH	74.12	25.88	54.26	45.74

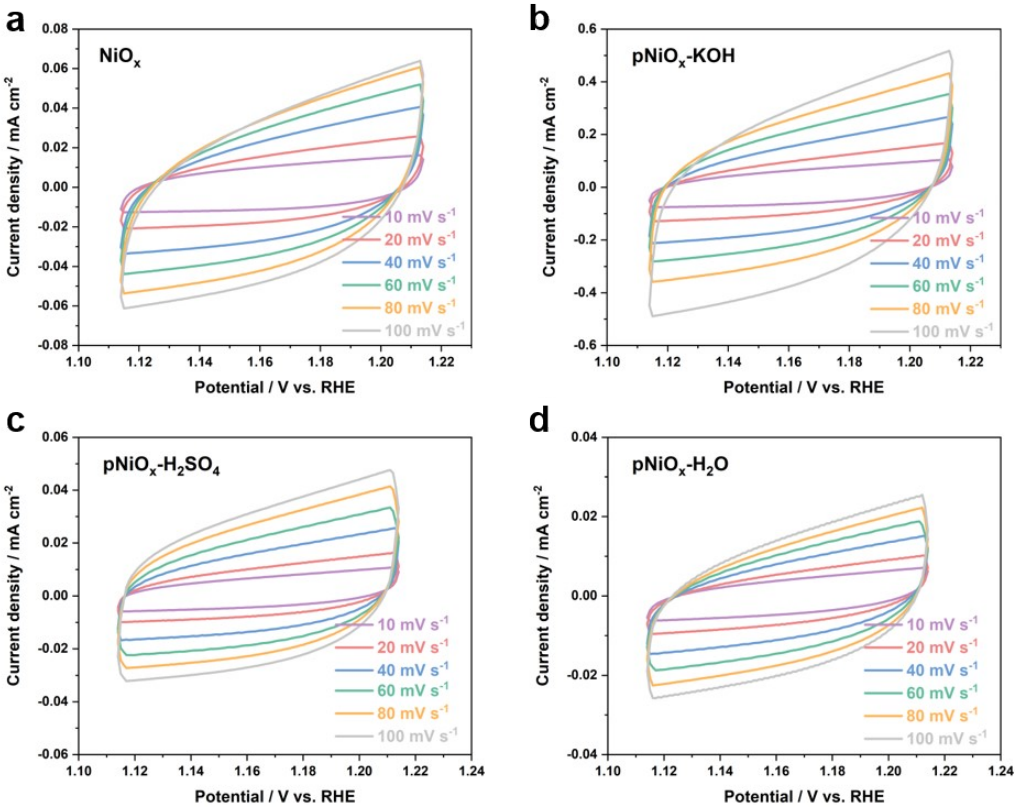

Fig. S7 CV curves of (a) NiO_x, (b) $pNiO_x$-KOH, (c) $pNiO_x$-H_2SO_4, and (d) $pNiO_x$-H_2O.

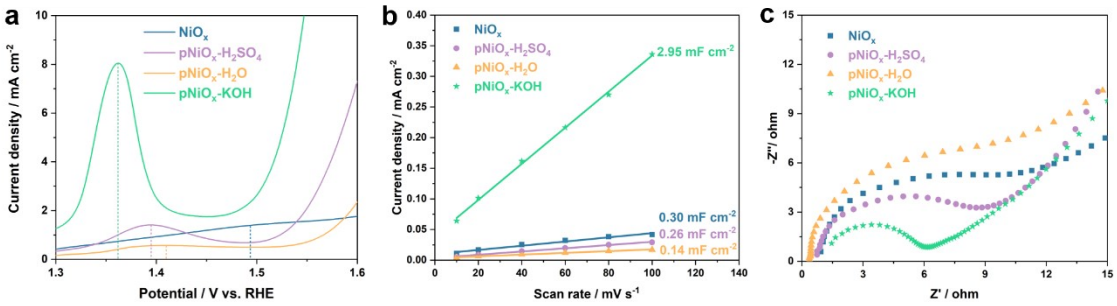

Fig. S8 (a) LSV curve, (b) C_{dl}, and (c) EIS of NiO_x, $pNiO_x$, $oNiO_x$, and $rNiO_x$.

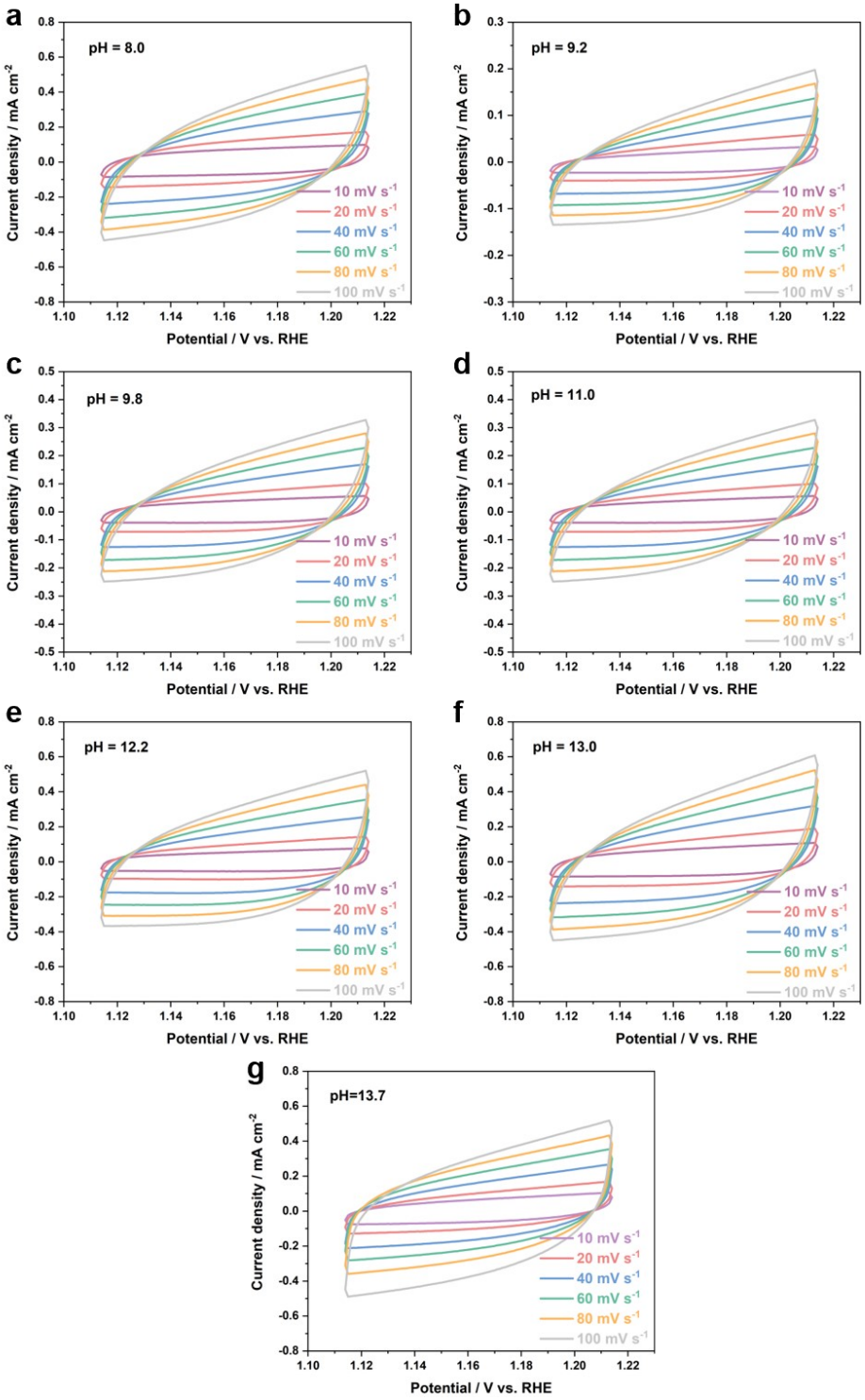

Fig. S9 Surface reconstruction of NiO_x under pulsed potential application in KOH solutions with varying pH values. The CV curves of the resulting $pNiO_x$ catalyst measured in 1 M KOH solution.

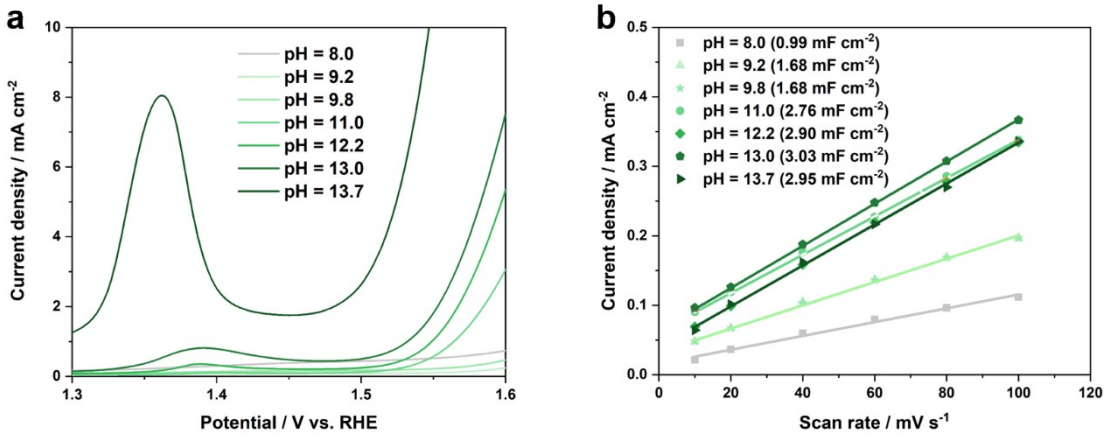

Fig. S10 Surface reconstruction of NiO_x under pulsed potential application in KOH solutions with varying pH values. (a) LSV curves and b) C_{dl} of the resulting $pNiO_x$ in 1 M KOH electrolyte.

To further investigate the pH-dependent reconstruction behavior of NiO_x, pulsed potentials were applied to NiO_x in KOH solutions with varying concentrations. The resulting $pNiO_x$ catalyst was evaluated through CV (Fig. S9) and LSV (Fig. S10a) measurements in 1 M KOH solution. As the pH increased from 8.0 to 13.7, the oxidation barrier of the generated $Ni(OH)_2$ progressively decreased, reflecting the enhanced adsorption capability of NiO_x toward oxygen-containing intermediates during OER processes. Moreover, the C_{dl} (Fig. S10b, derived from the fitting of Fig. S9) reached its maximum at pH ≈13.0, suggesting the exposure of abundant active sites. These results demonstrate that OH^- promotes the reconstruction of NiO_x, effectively optimizing its surface state to maximize the number of exposed active sites.

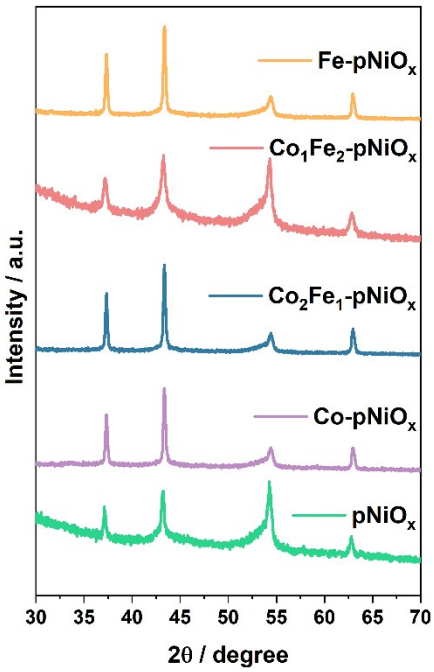

Fig. S11 XRD patterns of Co-pNiO$_x$, Co$_1$Fe$_2$-pNiO$_x$, Co$_2$Fe$_1$-pNiO$_x$, Fe-pNiO$_x$, and pNiO$_x$. There are no peak shifts in Co/Fe-doped pNiO$_x$ compared to pristine pNiO$_x$, indicating that Co and Fe are not incorporated into the lattice.

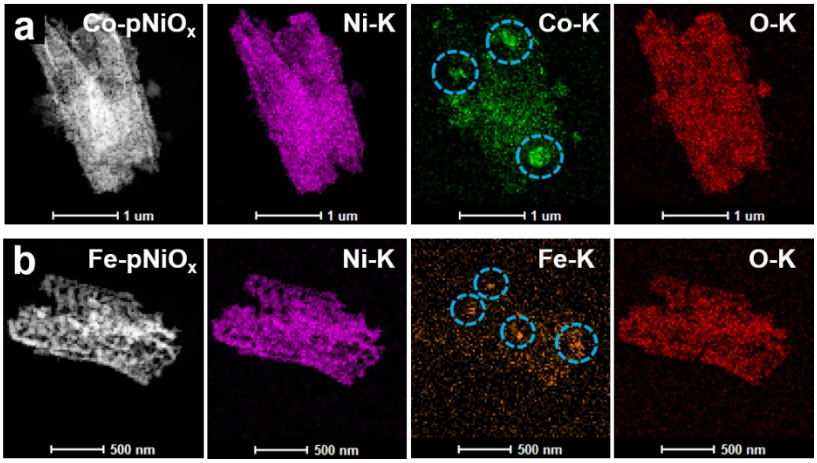

Fig. S12 EDS elemental mapping of (a) Co-pNiO$_x$ and (b) Fe-pNiO$_x$.

Table S4 EDS data of Co_2Fe_1-$pNiO_x$, Co-$pNiO_x$, and Fe-$pNiO_x$.

	Ni %	O %	Co %	Fe %
Co_2Fe_1-$pNiO_x$	64.54	33.50	0.56	1.37
Fe-$pNiO_x$	48.06	51.53	/	0.40
Co-$pNiO_x$	45.35	50.27	4.36	/

Table S5 ICP data of Co_2Fe_1-$pNiO_x$, Co-$pNiO_x$, and Fe-$pNiO_x$.

	Ni %	Co %	Fe %
Co_2Fe_1-$pNiO_x$	63.25	10.38	26.37
Fe-$pNiO_x$	87.53	/	12.47
Co-$pNiO_x$	68.31	31.68	/

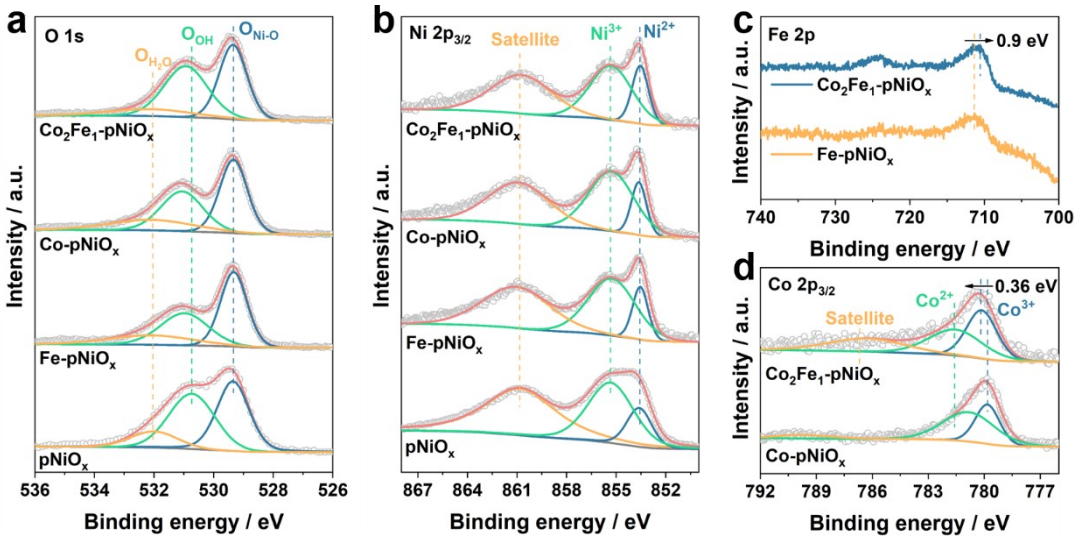

Fig. S13 (a) O 1s spectra and (b) Ni $2p_{3/2}$ spectra of $pNiO_x$, Co_2Fe_1-$pNiO_x$, Co-$pNiO_x$, and Fe-$pNiO_x$. (c) Fe 2p spectra of Co_2Fe_1-$pNiO_x$ and Fe-$pNiO_x$. (d) Co $2p_{3/2}$ spectra of Fe-$pNiO_x$ and Co-$pNiO_x$.[2]

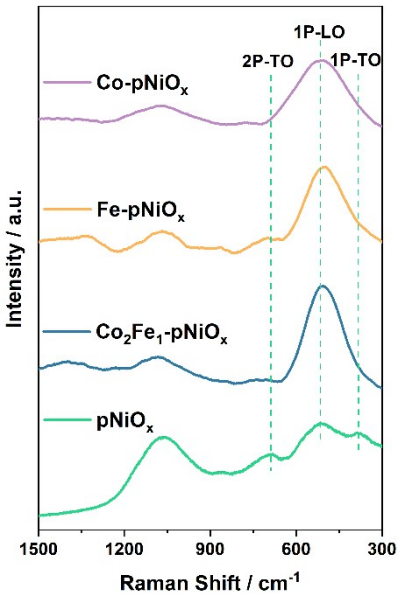

Fig. S14 Raman spectra of Co-pNiO$_x$, Co$_2$Fe$_1$-pNiO$_x$, Fe-pNiO$_x$, and pNiO$_x$.

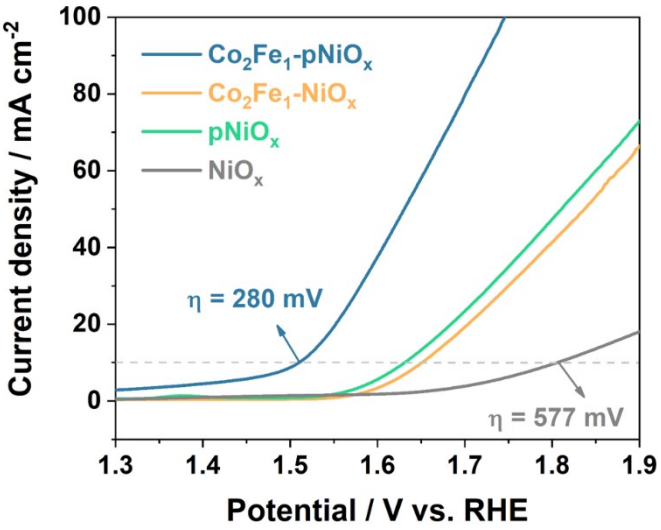

Fig. S15 The LSV curves of NiO_x, $pNiO_x$, Co_2Fe_1-NiO_x, and Co_2Fe_1-$pNiO_x$ catalysts tested in 1 M KOH.

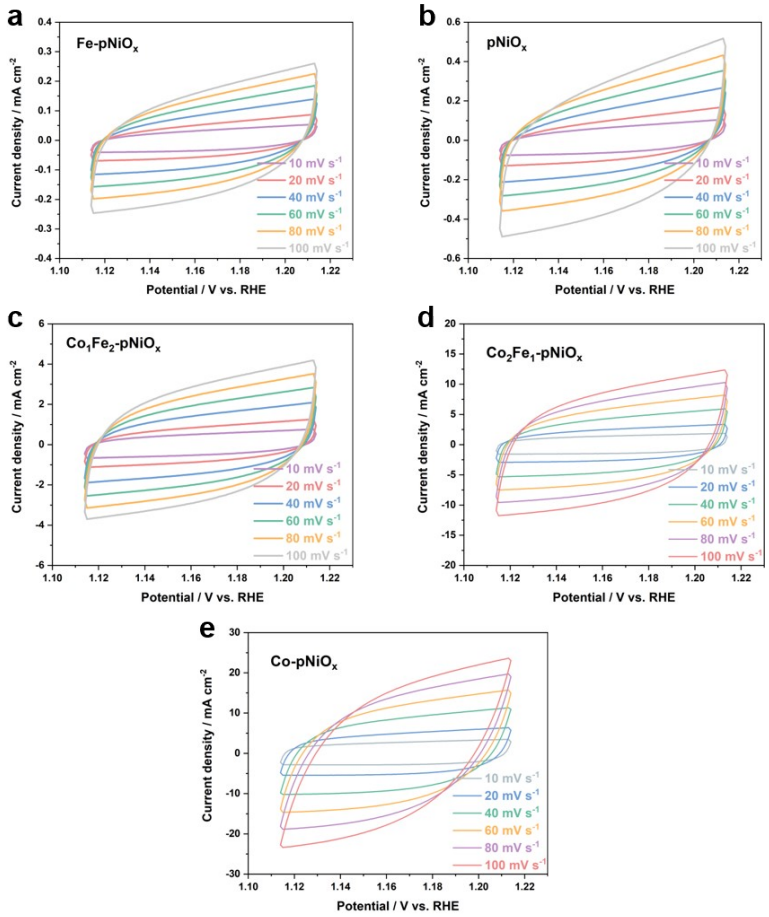

Fig. S16 The CV curves of the (a) Fe-$pNiO_x$, (b) $pNiO_x$, (c) Co_1Fe_2-$pNiO_x$, (d) Co_2Fe_1-$pNiO_x$, and (e) Co-$pNiO_x$ catalysts measured in 1 M KOH solution.

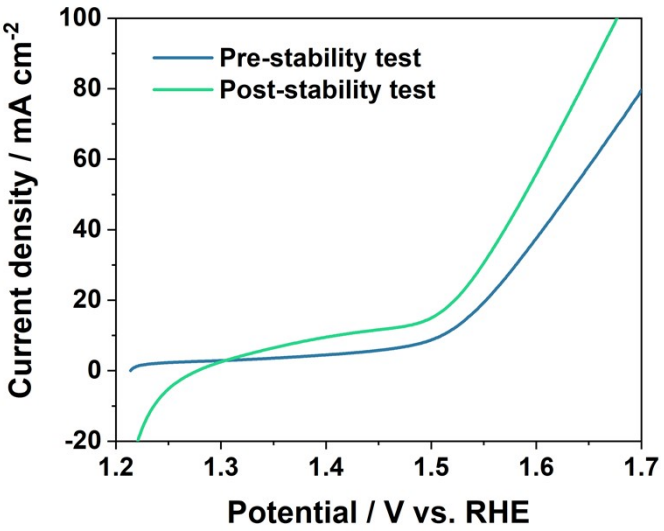

Fig. S17 The LSV curves before (Pre-stability test) and after (Post-stability test) stability testing.

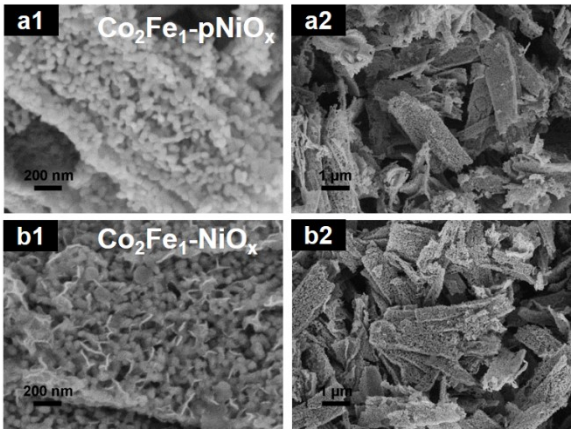

Fig. S18 SEM images of (a) Co_2Fe_1-$pNiO_x$ and (b) Co_2Fe_1-$pNiO_x$.

Reference

1 Z. Yue, W. Zhu, Y. Li, Z. Wei, N. Hu, Y. Suo and J. Wang, *Inorg. Chem.*, 2018, **57**, 4693–4698.
2 L. Ge, H. Yang, J. Guan, B. Ouyang, Q. Yu, H. Li and Y. Deng, *Inorg. Chem.*, 2023, **62**, 15664–15672.